



Photonic metamaterial with a subwavelength electrode pattern

GUILLAUME CROES,^{1,2,*} RENAUD PUYBARET,¹ JANUSZ BOGDANOWICZ,¹ UMBERTO CELANO,^{1,3} ROBERT GEHLHAAR,¹ AND JAN GENOE^{1,2}

¹imec, Sensors and Actuators Technology (SAT) Department, Kapeldreef 75, 3001 Leuven, Belgium

²Electrical Engineering Department (ESAT), Katholieke Universiteit Leuven, 3001 Leuven, Belgium

³School of Electrical, Computer and Energy Engineering, Arizona State University, Tempe, Arizona 85287, USA

*Guillaume.Croes@imec.be

Received 5 December 2022; revised 20 January 2023; accepted 9 February 2023; posted 9 February 2023; published 17 March 2023

The next generation of tunable photonics requires highly conductive and light inert interconnects that enable fast switching of phase, amplitude, and polarization modulators without reducing their efficiency. As such, metallic electrodes should be avoided, as they introduce significant parasitic losses. Transparent conductive oxides, on the other hand, offer reduced absorption due to their high bandgap and good conductivity due to their relatively high carrier concentration. Here, we present a metamaterial that enables electrodes to be in contact with the light active part of optoelectronic devices without the accompanying metallic losses and scattering. To this end, we use transparent conductive oxides and refractive index matched dielectrics as the metamaterial constituents. We present the metamaterial construction together with various characterization techniques that confirm the desired optical and electrical properties. © 2023 Optica Publishing Group

<https://doi.org/10.1364/AO.481396>

1. INTRODUCTION

Large area photonic devices as metasurfaces, optical phased arrays, and spatial light modulators (SLMs) have shown excellent control over incident light, whether waveguide-fed or plane-wave-illuminated. Their large degree of freedom is unique and enables them to bring new perspectives to applications such as wavefront shaping and holography [1]. They achieve these feats due to careful design of the modulators that influence phase, amplitude, and polarization. Evidently, a vast array of technologies, including thermo-optics [2], micro-electromechanical systems [3,4], liquid crystals [5,6], and phase-change materials [7,8], are being explored to enable fast and reliable modulator switching. Some of these state-of-the-art devices, such as metasurfaces, cannot be switched, while others are currently controlled optically [9,10]. In either case, electrical modulation is preferred for more robust switching. However, even when devices are electrically tunable, doing this over a large area remains a challenge due to the combination of electrode losses and desired modulator size. This is due to the link between the attainable field of view and the modulator or pixel size, which states that accurate control spanning over a 180° viewing angle requires subwavelength modulation. Hence, factoring in the refractive index of the modulator, light modulation needs to occur at scale of 100 nm or less. Consequently, a similar size restriction exists for the accompanying driving electronics needed to individually address each modulator. Due to the sheer number ($> 1E7/\text{mm}^2$) of modulators that need switching, the

most common approach would be to create metallic interconnects that introduce significant parasitic losses into the devices, leading to reduced efficiency.

It is well known that metallic electrodes can impede the operation of photonic, optoelectronic, and plasmonic devices such as LEDs, liquid crystal cells, and waveguide modulators due to their strong light–matter interaction [11,12]. This behavior stems from their high carrier concentration, which leads to a high conductivity but also to a high absorption due to the unbound nature of conduction electrons. The lowered performance can be avoided by taking special care with the device design. In practice, this often results in physically separating the metal from the active region, which is not an ideal solution for high modulator densities. Alternatively, a wide range of materials is being considered to replace metals as electrodes, including transparent conducting oxides (TCOs) and diluted metals [13–16].

Transparent conductive oxides form a group of materials that are easily deposited, CMOS-compatible, highly optically tunable [17], and have carrier densities similar to highly doped semiconductors [18], hence well below those of metals. On top of that, they are semitransparent to transparent due to their high bandgap and have been extensively used in thin-film devices as LEDs and touch screens. Nowadays, these material are becoming more widespread, finding uses in metasurfaces [19–22], epsilon-near-zero materials [23–25] and electro-optical modulators [26–28]. TCOs are often used in tandem with metals due

to their nonnegligible ohmic losses. Hence, they typically form a bridge between the light active region of the device and the peripheral electrical circuitry. However, in periodic structures, such as tunable metasurfaces and SLMs, TCOs are typically not index-matched with their surrounding materials. This again leads to undesired scattering of incident light, depending on the grating formed by the periodic TCO.

Here, we present a metamaterial that employs a TCO together with an index-matched dielectric such that electric bias can be applied directly to the active light region. Additionally, this metamaterial can be used as cladding layer in integrated photonics, since the material optically behaves isotropically in the chosen light range. The employed electrode scale allows subwavelength and individual electrode modulation in the visible range, resulting in a 180° viewing angle without any ghost images or scattering artifacts. Consequently, the created metamaterial enables the creation of high-density tunable modulators for transmission, reflection- or waveguide-based applications such as a holographic display. We showcase the required fabrication techniques and give insight in the optical and electrical properties by ellipsometry, scatterometry, rigorous coupled wave analysis (RCWA) and conductive atomic force microscopy (C-AFM).

2. METAMATERIAL DESIGN AND FABRICATION

A metamaterial was designed to provide the electrical bias required for a waveguide-based SLM. To that end, three criteria were kept in mind, namely, (1) steering over a 180° range is enabled; (2) no light scattering due to a refractive index difference between the electrode and dielectric material; and (3) no or limited influence from the remaining metallic components.

First, ensuring a device can steer over the full 180° range requires a modulation at half the size of the desired wavelength (diffraction grating). However, since the envisioned device is waveguide-based, the required modulation is linked to the internal wavelength. Hence, it is the effective refractive index of the guided mode of the envisioned SLM that determines the pitch of these subwavelength electrodes. A well-confined mode calls for a waveguide refractive index that is higher than the cladding materials. For common strong electro-optic materials, such as lithium niobate (LiNbO_3) and barium titanate (BaTiO_3), an electrode pitch of 90 nm practically covers the entire visible spectrum [29–31].

Second, it is the optical properties of the constituent materials of the metamaterial that determine whether Bragg scattering

can occur. Figure 1(a) shows a schematic of the envisioned metamaterial. Several TCOs were considered, including indium tin oxide (ITO), aluminum doped zinc oxide (Al:ZnO), and indium gallium zinc oxide (IGZO). Since atomic layer deposition (ALD) was needed for uniform filling, only ITO and IGZO were at hand in our fab. IGZO was preferred over ITO, since it is known to have a lower intrinsic carrier concentration that suits the intended application, as it does not require high switching speeds (video rate), while simultaneously lowering parasitic absorption. For other applications, such as optical I/O, ITO can result in faster switching at the cost of slightly higher optical losses. Silicon nitride (SiN) was paired to IGZO as dielectric, since it is semiconductor fab-compatible, easily deposited, and tunable over the same refractive index range. We used an IGZO recipe that has proven to yield good conductivity, to which we index-matched SiN to ensure the desired electrical properties [32,33]. This is beneficial, since at wavelengths where both refractive indices match, their combination will behave isotropically. On top of that, even if a small refractive index difference exists, the small electrode pitch leads to reduced Bragg scattering, since only higher order, and thus weaker scattering can take place.

Finally, to limit undesired absorption from metallic backplane components, the metamaterial is preferred to be as thick as possible to separate the waveguide physically from any metals. However, for ease of manufacturing the aspect ratio (AR) (depth/width) of the electrode pillars cannot be excessively large. The metamaterial was thus made 500 nm thick, resulting in an easily reproducible metamaterial with an AR close to 11.

In practice, the metamaterial waveguide cladding layer is created as follows. First, a TiN/tungsten back contact on SiO_x with critical dimension 50 nm is created using a damascene process: 300 nm SiO_x deposition on Si substrate, lithography 193 nm immersion with BARC and positive-tone resist, 100 nm etch of SiO_x , 10 nm TiN ALD, 200 nm W fill, and chemical-mechanical polishing (CMP) for planarization. Afterwards, the metamaterial is created by depositing a thick SiN layer (500 nm), which is then subjected to a high AR etch to open 45 nm-sized holes with 90 nm pitch. ALD is subsequently used to fill the SiN holes. Due to ALD's structure filling capabilities, a conformal IGZO fill can be achieved along the whole pillar, as shown in Figs. 1(b) and 1(c). CMP is used to remove the excess IGZO from the top and planarize the metamaterial. During planarization, a small amount of the metamaterial is consumed, resulting in a layer thickness of around 420 nm. This entire process is done in imec's CMOS 300 mm fab. A

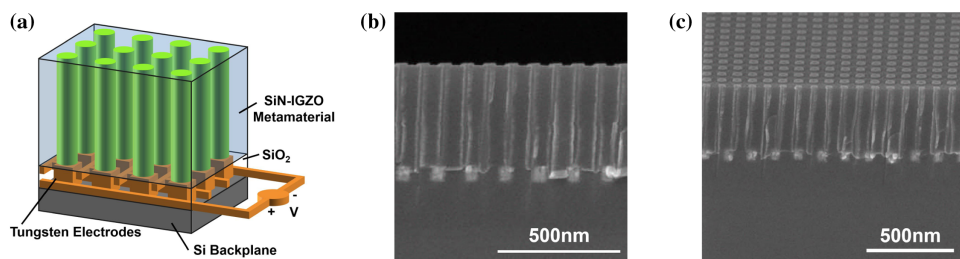


Fig. 1. (a) Schematic of the metamaterial; (b) cross-sectional SEM image; (c) angled top down SEM image.

post-process anneal in an O₂ rich environment at 250°C for an hour enables the IGZO conductivity through the creation of oxygen vacancies [34].

3. RESULTS AND DISCUSSION

A. Optical Characterization

Optical characterization was performed on planar layers (ellipsometry) and on the finished metamaterial (scatterometry and RCWA) to gain insight into their refractive indices and structural parameters, respectively.

1. Ellipsometry

The optical properties of the constituent materials are shown in Figs. 2(a) and 2(b). Ellipsometric measurements (Woollam RC2) were performed on planar layers, after which the data were fitted using a Tauc–Lorentz oscillator for SiN and a combination of Tauc–Lorentz and Drude oscillators for IGZO and the metamaterial. Here, the Tauc–Lorentz oscillator represents the amorphous nature of both SiN and IGZO, and the Drude oscillator is employed to fit IGZO’s metallic infrared absorption [35,36].

Table 1. SiN TL

SiN Tauc–Lorentz (TL)		Amp (eV)	Eo (eV)	Br (eV)	Eg (eV)
Parameter	Value	57.5564	7.422	5.951	2.654

To limit the present degrees of freedom, as both IGZO and SiN are highly tunable materials depending on their deposition parameters, a previously optimized recipe for high conductivity IGZO was used [32,33]. The fitting parameters for IGZO can be found in Table 1. Its resistivity, 0.003681 Ωcm, extracted from the Drude oscillator is similar to the resistivity of a weakly conducting semiconductor. This approach ensures the desired electrical properties and only requires SiN to be varied by altering its deposition parameters, influencing its stoichiometry and density, until its real refractive index matches well in the visible (440–640 nm), as indicated in Figs. 2(a) and 2(b), thus limiting the number of required blanket wafers. The total measured SiN range (light blue) as well as the closest matching SiN wafer (black) is shown in Figs. 2(a) and 2(b). Its fitting parameters are shown in Table 2. All ellipsometry measurements, including the full SiN range can be found in Data File 1.

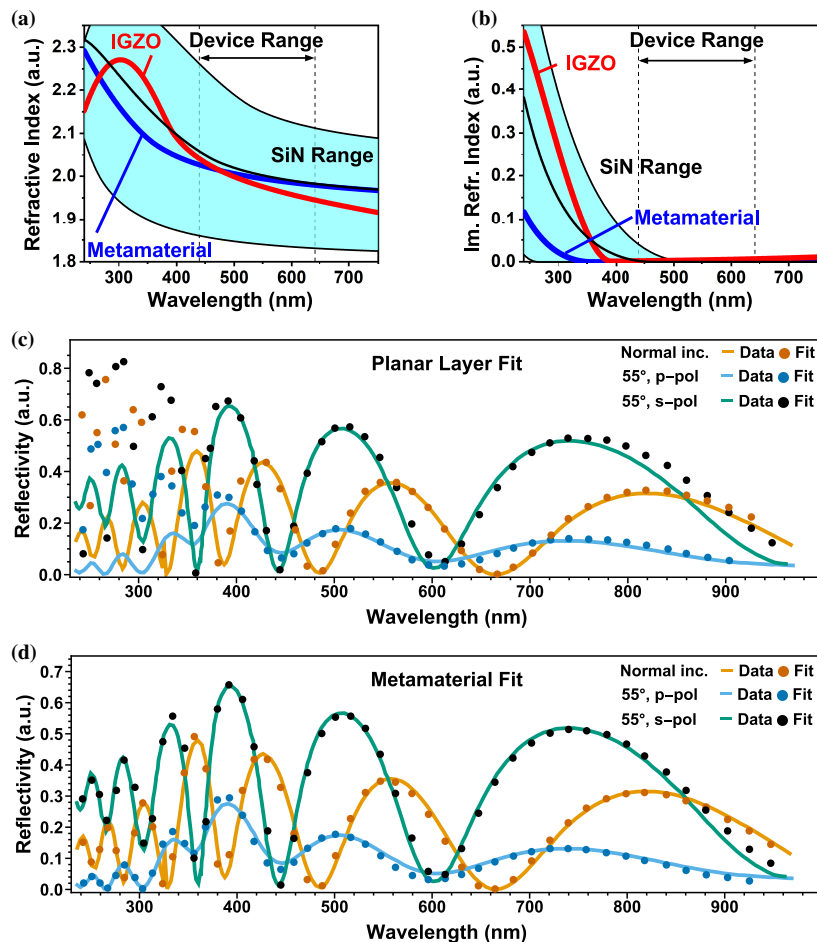


Fig. 2. (a) Refractive index (n) data of the metamaterial and their constituent materials measured by ellipsometry; (b) refractive index (k) data of the metamaterial and their constituent materials measured by ellipsometry; (c) scatterometry measurement fitted with a planar layer model; (d) scatterometry measurement fitted with a model having embedded pillar electrodes.

Table 2. IGZO TL

IGZO TL	Amp (eV)	Eo (eV)	Br (eV)	Eg (eV)
Value	118.5894	3.540	11.140	3.163
IGZO Drude	Resistivity ($\Omega \text{ cm}$)		Scattering Time (fs)	
Value	0.003681		2.096	

The completed metamaterial was initially fitted with the three oscillators expected for a blend of both materials (two Tauc–Lorentz and one Drude) and constrained to a thickness of 420 nm measured by SEM. Unfortunately, this model does not result in a good fit, as one of the Tauc–Lorentz oscillators yields unrealistic values. The best possible fit, shown in Table 1 of the [Supplement 1](#), was achieved by using only one Tauc–Lorentz oscillator, for which the refractive indices are shown in Figs. 2(a) and 2(b). That said, even for this best case scenario, the metamaterial fit remains rather poor and yields an imaginary refractive index that does not align with its constituents. The fit worsens when the thickness is included as a fitting parameter. Here, the model gives a significantly lower refractive index (both real and imaginary), paired with a larger thickness of 460 nm. (See [Supplement 1](#)). This is a rather unrealistic result, indicating that the inclusion of IGZO inside a SiN matrix can no longer be fitted with an isotropic model. It should, however, not be a surprise that an anisotropic metamaterial can not be fitted with an isotropic model. In fact, only at the wavelength where the two materials are equal can an isotropic model succeed. Evidently, a more advanced optical model is needed to extract correct parameters, for which we look toward scatterometry and Mueller matrix (MM) measurements.

2. Scatterometry

Scatterometry measurements (Nova T600 MMSR) and fits (Nova Mars) were performed on the finished metamaterial, shown in Figs. 2(c) and 2(d). The earlier mentioned refractive indices were used as input to extract the parameters of the embedded IGZO electrode in the SiN matrix.

Figure 2(c) shows the measured data (full line) and a structural fit (points) that represent the metamaterial by a single SiN layer without embedded electrodes. The fit indicates that this unpatterned layer should be 411 nm thick, which aligns well with the SEM data. For all wavelengths above 400 nm, the model corresponds well with the measured data. At wavelengths below 400 nm, due to the growing difference in SiN and IGZO refractive indexes, we are not expecting to obtain a fit in that spectral range. Figure 2(d) shows the same measurement data, now fitted with a model that assumes a SiN layer with embedded IGZO electrodes. The fit indicates a metamaterial thickness, pillar height, and pillar width of 408, 423, and 74 nm, respectively. For this second model, the complete wavelength range was fitted well, showcasing that the created metamaterial matches with the design and the measured SEM data. An overview of the scatterometry fitting parameters is shown in Table 3.

Table 3. Overview of Metamaterial Structural Parameters Fitted by Scatterometry

Model	Thickness (nm)	Pillar Width (nm)
SEM	420	45 nm
Ellipsometry	420–460	NA
Scatterometry (planar layer)	411	NA
Scatterometry (metamaterial fit)	408–423	74

3. RCWA

RCWA models were created, and their structural parameters were fit to averaged MM ellipsometry measurements (Woollam RC2, averaged from 30 measurements at 75° incidence). The ellipsometry data from Fig. 2 were used as input during the fits. A fitting algorithm was created, based on pySCATMECH for calculating MMs and a robust least square (LSQ) fitting function for optimizing the model [37,38]. The LSQ functions $F(\mathbf{x})$ is defined as

$$F(\mathbf{x}) = \sum_{j=1}^m \frac{(y_j - f_j(\mathbf{x}))^2}{\sigma_j^2}. \quad (1)$$

Here, \mathbf{x} is a vector representing the RCWA structural parameters, y_j represents the measured MM data points at the j th wavelength, $f_j(\mathbf{x})$ are the calculated data points by the RCWA model, and σ_j^2 is the variance of 30 separate measurements. Figure 3(a) shows a schematic of the RCWA models that were fitted to the measured MM data. Two fits were made with: (1) a model based on a single SiN layer and (2) a model that assumes the metamaterial has 45 nm-sized embedded electrodes in a SiN matrix having a 90 nm pitch. The pillar width and pitch were not fitted, since the model has only a negligible sensitivity to them. (See [Supplement 1](#)) The fits and measured MM data are shown in Fig. 3(b). It should be noted that MM data are usually normalized to the first element (MM11) and that there are eight zero elements due to the symmetry of the measured metamaterial structure [39].

For model 1, a good fit with an LSQ value of 4132 was achieved, resulting in a thickness of 422 nm, proving accurate calculation of the MM data and matching well with our SEM data. For model 2, which matches the designed ideal metamaterial (45 nm electrodes with 90 nm pitch), an LSQ value of 5797 was found at a thickness of 424 nm compared to model 1. Clearly, both models fit the thickness of the metamaterial well. (See Table 4). The closely matching LSQ values confirm the isotropic nature of the metamaterial. See [Supplement 1](#) for the LSQ values for various fitted metamaterial heights.

B. Electrical Characterization

To prove the conductivity of the metamaterial, C-AFM measurements were performed. Figure 4 shows a comparison between an atomic force microscopy (AFM) and C-AFM measurement. AFM data confirm that the electrode pillar slightly (~ 11 nm) extrudes from the metamaterial after planarization, which aligns well with our SEM data. Figure 4(b) shows

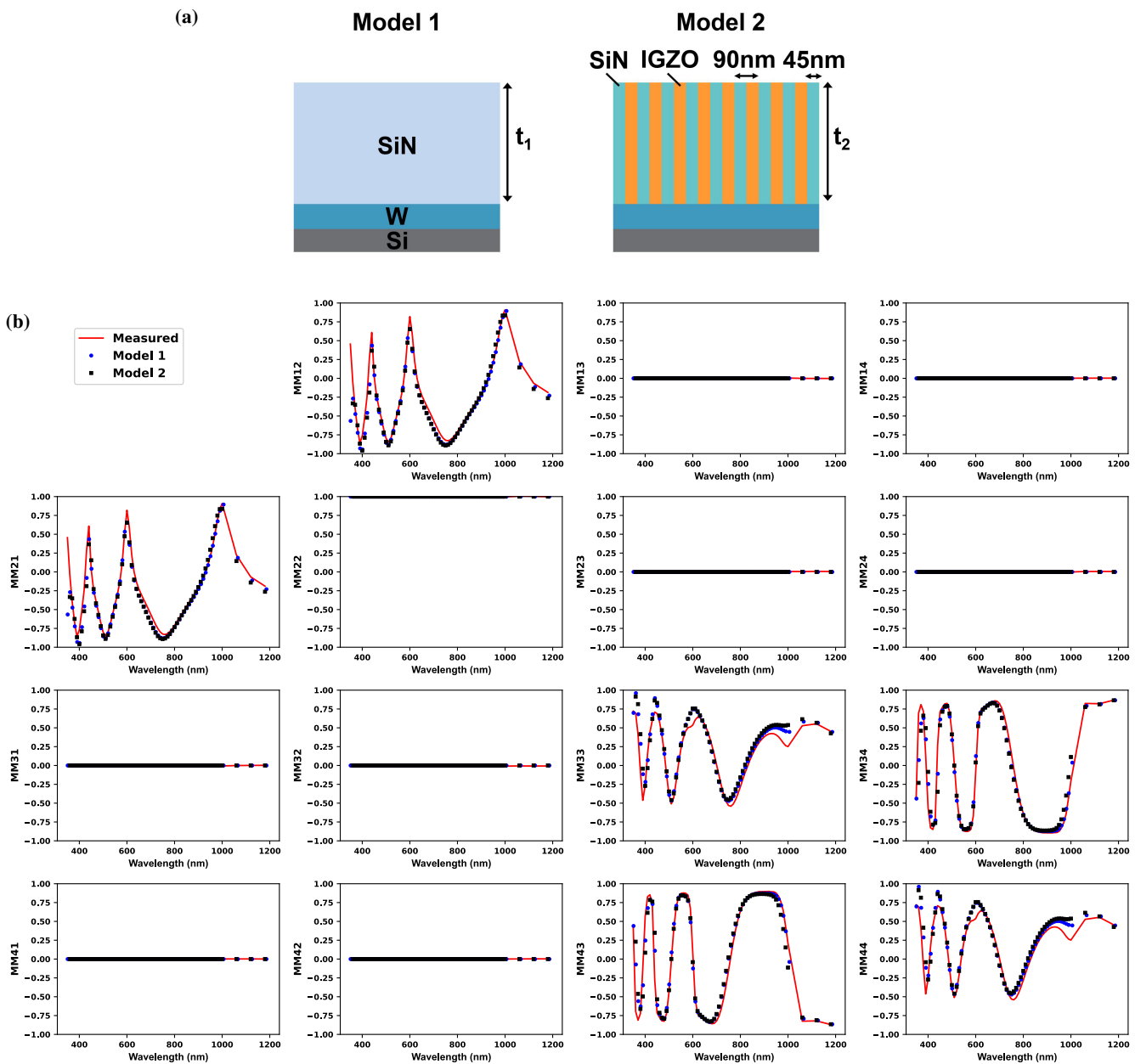


Fig. 3. (a) Schematic of the RCWA model assuming the metamaterial is an effective medium; (b) schematic of the RCWA model having IGZO pillars embedded in SiN; (c) MM measurement and fits of the various models shown in (a) and (b).

Table 4. Overview of Metamaterial Structural Parameters Fitted by RCWA Simulations

Model	Thickness (nm)	Pillar Width (nm)
SEM	420	45 nm
Ellipsometry	420–460	NA
RCWA (planar fit)	422	NA
RCWA (metamaterial fit)	424	no sensitivity

a schematic of the electric loop connecting the back contact, pillar electrodes, and the C-AFM. Here, a nanosized conductive probe is scanned in direct contact with the sample surface, while a voltage is applied between the tip and the sample. Note that although the probe is scanning the surface in direct contact, a

relatively high tip–sample contact resistance exists between the tip and the IGZO, resulting in low detectable leakage (i.e., in the pA range). Furthermore, the observed conduction is linked to a convolution of all the present resistive terms. Hence, this is a combination of the electrode pillar, the metallic back contact, and the Si substrate. Consequently, the dominant resistance is not the tip–sample junction, and the absolute value of current measured should only be considered in relative terms. Additionally, local fluctuations must be ascribed to small surface modifications of the IGZO top surface, such as stoichiometry variations or intragrain scattering that can locally make the resistance of the tip–sample junction dominant. Figure 4(c) shows current flowing at the tip–sample junction when scanning with 6 V bias over an area of $0.8 \times 0.8 \mu\text{m}^2$. Clear contrast

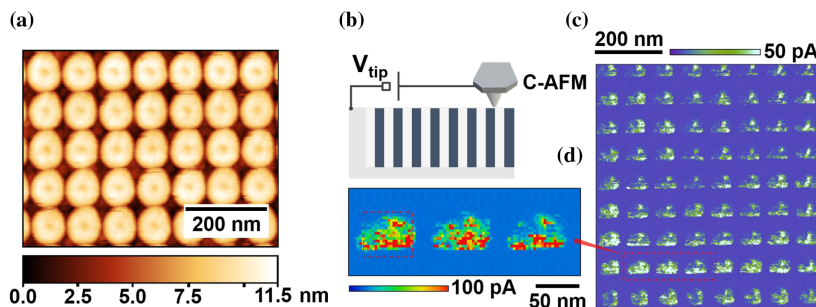


Fig. 4. (a) Relative height image of metamaterial by atomic force microscope; (b) schematic of conductive atomic force microscope operation; (c) current map of individual metamaterial pillars by conductive atomic force microscope; (d) high-resolution conductive atomic force microscope image of the metamaterial.

is visible corresponding to IGZO, indicating a lower resistance path for current in these locations and thus confirming the electrode conductivity. The observed nonround pillar shape is likely linked to the larger than normal employed C-AFM tip pressure in an attempt to minimize the tip–sample resistive junction. Consequently, the slightly triangular shape is clearly the result of a truncated probe scanned at high pressure, thus losing the high AR of a pristine conductive probe. Higher resolution C-AFM imaging is reported in Fig. 4(d), where three IGZO pillars are sensed. The results indicate that the electrical properties of the IGZO pillars are not uniform, with clear variations of the measured leakage with fluctuations in the range of 10–20 nm. These are attributed to local structural and compositional variations.

4. CONCLUSION

We have presented a metamaterial electrode cladding layer designed for waveguide-based optical modulators. Three criteria were identified that make for an excellent electrode cladding. Hence, no metals were used close to the active region, a sub-wavelength electrode pitch was used, and Bragg scattering was avoided by refractive-index-matching the constituent materials, namely, SiN and IGZO. We have shown ellipsometry measurements and fits of the metamaterial and its constituents and conclude that it behaves optically isotropic over the visible range. We find that standard ellipsometry oscillators result in a poor fit on the metamaterial, evident from its lower than expected imaginary refractive index. This problem is exacerbated when the thickness is included as a fitting parameter, resulting in a thicker layer with a lowered real refractive index. On the other hand, scatterometry, and MM RCWA measurements confirm the dimensions of the embedded pillars and the metamaterial, respectively. AFM indicates that the pillar electrodes extrude slightly from its SiN matrix, and C-AFM confirms the conductivity of the pillar electrodes. A similar fabrication scheme can be used with alternative materials expanding the capabilities of the metamaterial into different operating regimes, for example ITO can lead to faster switching speeds due to its higher carrier concentration compared to IGZO.

Funding. Fonds Wetenschappelijk Onderzoek (1S91520N); European Research Council (742299).

Disclosures. The authors have no conflicts of interest.

Data availability. Data underlying the results presented in this paper are available in Refs. [3],40.

Supplemental document. See Supplement 1 for supporting content.

REFERENCES

- Q. Jiang, G. Jin, and L. Cao, “When metasurface meets hologram: principle and advances,” *Adv. Opt. Photon.* **11**, 518 (2019).
- J. Sun, E. Timurdogan, A. Yaacobi, E. S. Hosseini, and M. R. Watts, “Large-scale nanophotonic phased array,” *Nature* **493**, 195–199 (2013).
- Z. Ren, Y. Chang, Y. Ma, K. Shih, B. Dong, and C. Lee, “Leveraging of MEMS technologies for optical metamaterials applications,” *Adv. Opt. Mater.* **8**, 1900653 (2020).
- W. M. Zhu, A. Q. Liu, X. M. Zhang, D. P. Tsai, T. Bourouina, J. H. Teng, X. H. Zhang, H. C. Guo, H. Tanoto, T. Mei, G. Q. Lo, and D. L. Kwong, “Switchable magnetic metamaterials using micromachining processes,” *Adv. Mater.* **23**, 1792–1796 (2011).
- S. Savo, D. Shrekenhamer, W. J. Padilla, S. Savo, D. Shrekenhamer, and W. Padilla, “Liquid crystal metamaterial absorber spatial light modulator for THz applications,” *Adv. Opt. Mater.* **2**, 275–279 (2014).
- Z. He, F. Gou, R. Chen, K. Yin, T. Zhan, and S.-T. Wu, “Liquid crystal beam steering devices: principles, recent advances, and future developments,” *Crystals* **9**, 292 (2019).
- F. Ding, Y. Yang, and S. I. Bozhevolnyi, “Dynamic metasurfaces using phase-change chalcogenides,” *Adv. Opt. Mater.* **7**, 1801709 (2019).
- S. Y. Lee, Y. H. Kim, S. M. Cho, G. H. Kim, T. Y. Kim, H. Ryu, H. N. Kim, H. B. Kang, C. Y. Hwang, and C. S. Hwang, “Holographic image generation with a thin-film resonance caused by chalcogenide phase-change material,” *Sci. Rep.* **7**, 41152 (2017).
- J. Hu, S. Bandyopadhyay, Y. H. Liu, and L. Y. Shao, “A review on metasurface: from principle to smart metadevices,” *Front. Phys.* **8**, 502 (2021).
- X. Zhao, Z. Sun, L. Zhang, Z. Wang, R. Xie, J. Zhao, R. You, and Z. You, “Review on metasurfaces: an alternative approach to advanced devices and instruments,” *Adv. Devices Instrum.* **2022**, 9765089 (2022).
- C. Cho, T. Antrack, M. Kroll, Q. An, T. R. Bärschneider, A. Fischer, S. Meister, Y. Vaynzof, and K. Leo, “Electrical pumping of perovskite diodes: toward stimulated emission,” *Adv. Sci.–Weinheim* **8**, 2101663 (2021).
- M. Ferrera, S. Saha, A. Boltasseva, V. M. Shalaev, and W. Jaffray, “Transparent conducting oxides: from all-dielectric plasmonics to a new paradigm in integrated photonics,” *Adv. Opt. Photon.* **14**, 148–208 (2022).
- V. E. Babicheva, A. Boltasseva, and A. V. Lavrinenko, “Transparent conducting oxides for electro-optical plasmonic modulators,” *Nanophotonics* **4**, 165–185 (2015).
- M. Dasog, “Transition metal nitrides are heating up the field of plasmonics,” *Chem. Mater.* **34**, 4249–4258 (2022).
- M. Gioti, J. Arvanitidis, D. Christofilos, K. Chaudhuri, T. Zorba, G. Abadias, D. Gall, V. M. Shalaev, A. Boltasseva, and P. Patsalas,

- "Plasmonic and phononic properties of epitaxial conductive transition metal nitrides," *J. Opt.* **22**, 084001 (2020).
16. G. V. Naik, V. M. Shalaev, and A. Boltasseva, "Alternative plasmonic materials: beyond gold and silver," *Adv. Mater.* **25**, 3264–3294 (2013).
 17. E. Feigenbaum, K. Diest, and H. A. Atwater, "Unity-order index change in transparent conducting oxides at visible frequencies," *Nano Lett.* **10**, 2111–2116 (2010).
 18. G. V. Naik, J. Kim, and A. Boltasseva, "Oxides and nitrides as alternative plasmonic materials in the optical range [Invited]," *Opt. Mater. Express* **1**, 1090 (2011).
 19. Y.-W. Huang, H. W. H. Lee, R. Sokhoyan, R. A. Pala, K. Thyagarajan, S. Han, D. P. Tsai, and H. A. Atwater, "Gate-tunable conducting oxide metasurfaces," *Nano Lett.* **16**, 5319–5325 (2016).
 20. J. Kim, S. Choudhury, C. DeVault, Y. Zhao, A. V. Kildishev, V. M. Shalaev, A. Alù, and A. Boltasseva, "Controlling the polarization state of light with plasmonic metal oxide metasurface," *ACS Nano* **10**, 9326–9333 (2016).
 21. J. Park, J.-H. Kang, S. J. Kim, X. Liu, and M. L. Brongersma, "Dynamic reflection phase and polarization control in metasurfaces," *Nano Lett.* **17**, 407–413 (2017).
 22. M. Y. Shalaginov, S. D. Campbell, S. An, Y. Zhang, C. Ríos, E. B. Whiting, Y. Wu, L. Kang, B. Zheng, C. Fowler, H. Zhang, D. H. Werner, J. Hu, and T. Gu, "Design for quality: reconfigurable flat optics based on active metasurfaces," *Nanophotonics* **9**, 3505–3534 (2020).
 23. R. W. Ziolkowski, "Propagation in and scattering from a matched metamaterial having a zero index of refraction," *Phys. Rev. E* **70**, 046608 (2004).
 24. I. Liberal and N. Engheta, "Near-zero refractive index photonics," *Nat. Photonics* **11**, 149–158 (2017).
 25. X. Niu, X. Hu, S. Chu, and Q. Gong, "Epsilon-near-zero photonics: a new platform for integrated devices," *Adv. Opt. Mater.* **6**, 1701292 (2018).
 26. H. W. Lee, G. Papadakis, S. P. Burgos, K. Chander, A. Kriesch, R. Pala, U. Peschel, and H. A. Atwater, "Nanoscale conducting oxide PlasMOStor," *Nano Lett.* **14**, 6463–6468 (2014).
 27. I. C. Reines, M. G. Wood, T. S. Luk, D. K. Serkland, and S. Campione, "Compact epsilon-near-zero silicon photonic phase modulators," *Opt. Express* **26**, 21594–21605 (2018).
 28. D. C. Zografopoulos, G. Sinatkas, E. Lotfi, L. A. Shahada, M. A. Swillam, E. E. Kriezis, and R. Beccherelli, "Amplitude modulation in infrared metamaterial absorbers based on electro-optically tunable conducting oxides," *Appl. Phys. A* **124**, 105 (2018).
 29. E. H. Turner, "High-frequency electro-optic coefficients of lithium niobate," *Appl. Phys. Lett.* **8**, 303–304 (1966).
 30. C. Wang, M. Zhang, B. Stern, M. Lipson, and M. Lončar, "Nanophotonic lithium niobate electro-optic modulators," *Opt. Express* **26**, 1547–1555 (2018).
 31. S. Abel, T. Stöferle, C. Marchiori, C. Rossel, M. D. Rossell, R. Erni, D. Caimi, M. Sousa, A. Chelnokov, B. J. Offrein, and J. Pompeyrene, "A strong electro-optically active lead-free ferroelectric integrated on silicon," *Nat. Commun.* **4**, 1671 (2013).
 32. S. Steudel, J. L. P. Van Der Steen, M. Nag, et al., "Power saving through state retention in IGZO-TFT AMOLED displays for wearable applications," *Dig. Tech. Pap. - SID Int. Symp.* **48**, 38–41 (2017).
 33. A. V. Glushkova, H. F. W. Dekkers, M. Nag, J. I. del Agua Borniquel, J. Ramalingam, J. Genoe, P. Heremans, and C. Rolin, "Systematic study on the amorphous, C-axis-aligned crystalline, and protocrystalline phases in In-Ga-Zn oxide thin-film transistors," *ACS Appl. Electron. Mater.* **3**, 1268–1278 (2021).
 34. A. de Jamblinne de Meux, A. Bhoopalakam, G. Pourtois, J. Genoe, and P. Heremans, "Oxygen vacancies effects in a-IGZO: formation mechanisms, hysteresis, and negative bias stress effects," *Phys. Status Solidi A* **214**, 1600889 (2017).
 35. G. E. Jellison and F. A. Modine, "Parameterization of the optical functions of amorphous materials in the interband region," *Appl. Phys. Lett.* **69**, 371–373 (1996).
 36. T. E. Tiwald, D. W. Thompson, J. A. Woollam, W. Paulson, and R. Hance, "Application of IR variable angle spectroscopic ellipsometry to the determination of free carrier concentration depth profiles," *Thin Solid Films* **313–314**, 661–666 (1998).
 37. T. A. Germer, "pySCATMECH: a Python interface to the SCATMECH library of scattering codes," *Proc. SPIE* **11485**, 114850J (2020).
 38. J. Zhu, S. Liu, X. Chen, C. Zhang, and H. Jiang, "Robust solution to the inverse problem in optical scatterometry," *Opt. Express* **22**, 22031–22042 (2014).
 39. O. Arteaga, "Useful Mueller matrix symmetries for ellipsometry," *Thin Solid Films* **571**, 584–588 (2014).
 40. G. Croes, R. Puybaret, J. Bogdanowicz, U. Celano, R. Gehlhaar, and J. Genoe, "Raw data from ellipsometry measurements," figshare (2023), <https://doi.org/10.6084/m9.figshare.21931824>.